© The Author 2009. Published by Oxford University Press
on behalf of Japanese Society of Microscopy. All rights reserved.
For permissions, please e-mail: journals.permissions@oxfordjournals.org
Journal of Electron Microscopy Advance Access published April 27, 2009
Journal of Electron Microscopy: 1–11 (2009)
doi: 10.1093/jmicro/dfp022

Special number: History/Review

Review of recent advances in spectrum imaging and its extension to reciprocal space

Alan Maigné[1,*] and Ray D. Twesten[2]

[1]Gatan Inc., 3F Sakurai Building, 2-8-19 Fukagawa, Koto-ku, Tokyo 135-0033, Japan and [2]Gatan, Inc., 5794 W. Las Positas Blvd., Pleasanton, CA 94588, USA
*To whom correspondence should be addressed. E-mail: amaigne@gatan.com

Abstract Using examples from various domains of science, this review covers some recent developments in spectrum imaging (SI) using scanning transmission electron microscopy (STEM) and electron energy loss spectroscopy (EELS). Advanced multi-dimensional acquisition methods allow the acquisition of STEM–EELS data with other complementary data such as energy dispersive X-ray spectroscopy (EDS), cathodoluminescence and even combining them with reciprocal space analysis through a new method called diffraction imaging. This method allows real and reciprocal space information to be mixed to get a more complete description of the electron–sample interaction. The developments in SI data analysis such as multiple linear least-squares fitting, non-linear least-squares fitting and multivariate analysis allow for a robust extraction not only of each elemental distribution but also of each chemical phase in a sample through an intuitive computer-assisted method.

Keywords EELS, diffraction imaging, spectrum Imaging, multivariate analysis, atomic resolution analysis, ELNES

Received 25 December 2008, accepted 14 April 2009

Introduction

Spectrum imaging (SI) is a powerful data acquisition approach for materials characterization whereby a spectrum is recorded at each pixel position in an image to form a 3D data set. As a technique, it is a powerful means for rapid materials characterization at the nanometer level and is well established, especially in the field of materials science [1–3]. Recently, the SI method has become even more powerful with the widespread availability of spherical aberration (Cs)-corrected scanning transmission electron microscopy (STEM) which allows a strong incident electron beam current in a sub-nanometer probe making atomic resolution analysis, such as shown on Fig. 1, possible [4].

To take the full advantage afforded by Cs-corrected STEM, we have developed new acquisition modalities, namely, sub-pixel scanning and multi-dimensional acquisition methods. Progress in electron microscopy has been made not only in aberration correction and probe current; combining advanced high-brightness electron sources and aberration-corrected EELS spectrometers, it is now routine to achieve an energy resolution below 1 eV with sufficient current to record many high-quality core-loss spectra each second, thus enabling routine fine-structure analysis of EELS spectra. As explained later in this review, each structure or chemical phase may have a characteristic EELS fingerprint corresponding to the shape of the spectrum. Multi-linear and non-linear least-squares fittings (MLLS and NLLS) are two powerful tools to identify and analyze these fingerprints. Multivariate analysis goes even further in the spectral analysis by identifying and mapping the spatial distribution of the phases in an experimental data set.

By extending the concept of SI to reciprocal space, one can see that instead of recording a single value or a one-dimensional (1D) spectrum at each image point in the sample, it is just as valid to acquire a 2D diffraction pattern at each data point creating what has been referred to as a diffraction image (DI). This technique allows the joint acquisition and analysis of data in both image (real) and diffraction (reciprocal) space. In this article, using different examples, we will review these acquisitions and analysis method and show how they can greatly improve and simplify analytical STEM experiments.

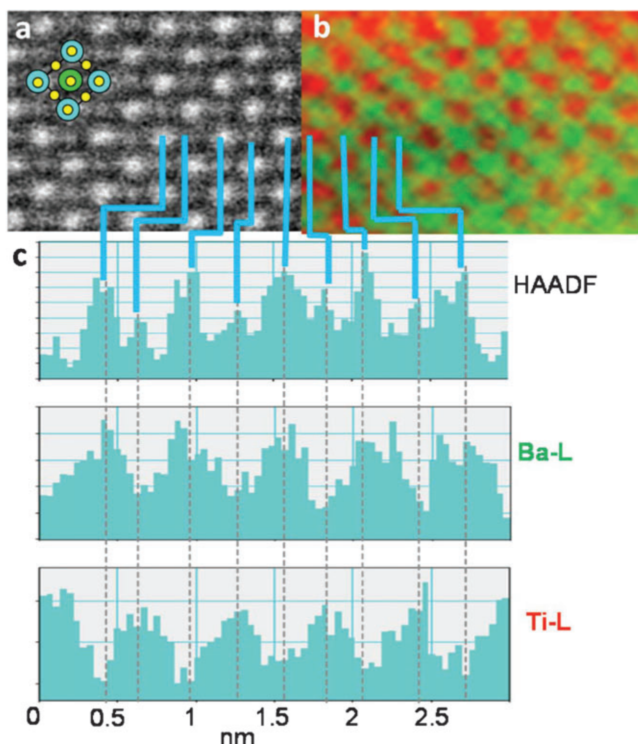

Fig. 1. STEM-EELS spectrum imaging analysis of $BaTiO_3$ using a Hitachi HD-2700 and a customized Gatan Enfina. (a) shows the HAADF image with an inset in the top left corner showing the expected atomic structure with titanium, barium and oxygen in green, blue and yellow. On the right, (b) shows the EELS elemental map (barium in green and titanium in red). (c) shows the intensity profiles of the HAADF signal and of the map of Ba and Ti obtained from the Ba–L and Ti–L peaks. We can clearly see that the white spots in the HAADF image (intense peak in the HAADF profile) correspond to barium and the gray spots to titanium. The atomic structure of the sample can be easily identified combining EELS with spectrum imaging with a resolution superior to 0.2 nm in this example.

Experimental details

EELS spectrometer

In a TEM, when primary electrons hit a material, they interact with the constituent atoms via electrostatic (Coulomb) forces, and some of them are scattered [5]. During the scattering, the direction of their momentum is changed, and in some cases, they transfer energy to the sample. Such inelastic scattering can be caused by phonon excitation, plasmon excitation or single-electron excitation. An EELS spectrum shows how many electrons (Y-axis) have lost a certain amount of energy (X-axis). The spectrum represents the transition to the unoccupied state in the material. The spectrum can be decomposed into three parts: the zero-loss peak represents unscattered or elastically scattered electrons; the low-loss region (5–30 eV) represents the excitation of electrons in the outermost atomic orbital, which are often delocalized due to interatomic bonding and extend over several atomic sites. This region reflects the solid-state character of the sample; the core-loss region (>30 eV) contains peak characteristics of the elemental composition of the sample.

By collecting the primary electrons and measuring their energy loss, we will obtain information about the plasmon excitations, the local density of states and the composition of the sample. An EELS spectrometer can disperse those electrons according to their energy and project them on a detector which can record the spectrum obtained as shown in Fig. 2.

Advanced multi-dimensional SI acquisition method

To obtain a spectrum for each point of the desired area, a digital scanning system can be used to position the beam on the sample while the spectrometer acquires the EELS data. The final obtained data are a tridimensional data set containing the EELS spectrum corresponding to each scanned point on the image [6].

Rapid increases in the computing power, increased ease of use and the advent of high-sensitivity and high-throughput detectors have enabled acquisition of higher dimensional data sets within a practical time-scale. Advances in control software and systems integration have allowed for simultaneously capturing multiple spectral signals such as annular dark field, secondary electrons or cathodoluminescence signals, as well as providing complementary information in a spatial correlation to these signals to further increase the ability of this technique. For example, combined EELS and EDS spectrum imaging is an effective approach for solving materials science problems, enabling quantitative concentration measurements for a wide range of elements to be obtained along with chemical state information [7].

Sub-pixel scanning method

Cs-corrected and FEG STEM systems have the ability to produce very small probes (below 1 Å for the most advanced instruments). Therefore, during the SI acquisition, it is very frequent that the SI pixel size is larger than the probe itself; this phenomenon is called under-sampling. By undersampling, the pixel information can be missed, resulting in inaccurate or misleading data as shown in Fig. 3. One solution to this problem is to sub-scan the probe over the pixels until all the area is covered. Moreover, this method presents a great advantage to reduce sample contamination and damage effects by reducing the time when the beam is stationary. For example, if the beam stays 0.5 s at each pixel, then that incident beam will be spread over the entire area of the pixel rather than just at the center, which will greatly reduce the dose for low-resolution scanning.

Diffraction imaging

By acquiring a diffraction pattern at each pixel position of a spectrum image, joint diffraction/image data are captured as information-rich 4D data sets which we call diffraction image (DI) stacks (Fig. 4). These DI stacks can be acquired

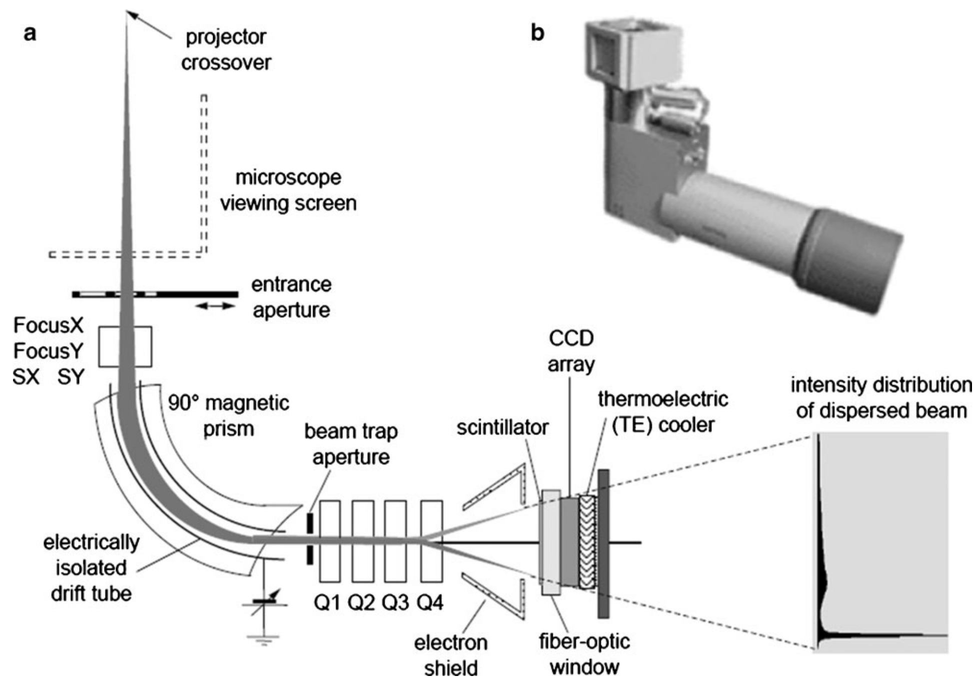

Fig. 2. Gatan Enfina EELS spectrometer. The schema (a) shows the electrons being dispersed in the magnetic prism and then projected onto the CCD via quadrupoles lenses. (b) shows a picture of the Gatan Enfina.

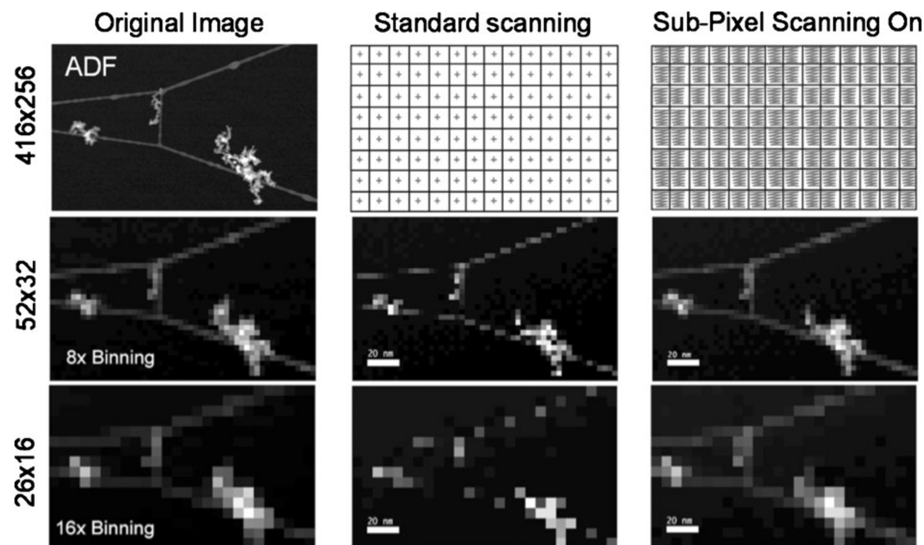

Fig. 3. Benefit of sub-pixel scanning on ADF images. The images on the left show ADF images obtained by scanning 416 points over 256 lines and the results of an 8 times and 16 times rebinning of that data. Using standard scanning (middle column), a 52 × 32 and especially a 25 × 16 acquisition should be the same as the binned 416 × 256 images if the probe is not smaller than the pixel size. Due to under-sampling, standard scanning shows artifacts such as missing particles and misleading geometrical structures. Using sub-pixel scanning (right column), the acquired images are more similar to the binned image, producing a faithful representation of the structures in the sample.

under the spectrum image (SI) paradigm allowing the full host of acquisition tools such as drift tracking and multi-signal acquisition to be utilized. The acquisition technique is completely generic; the only instrumental requirements are the STEM mode and a digital camera. One particularly powerful mode is the use of an energy filter to record a DI stack of energy-filtered diffraction patterns allowing the removal of plasmons scattering from diffraction greatly increasing the pattern contrast and interpretability.

This method can be used either in the spot mode with a small aperture to obtain a diffraction pattern or in a convergence beam electron diffraction (CBED) mode with a larger aperture. The measurement should be done with the sample at the eucentric height. The choice of the camera length is very important to obtain a field of view large enough to contain all the interesting data. However, one should keep in mind that such 4D sets are very large. For example, the size of a DI file composed of 256 × 256 real-space pixels

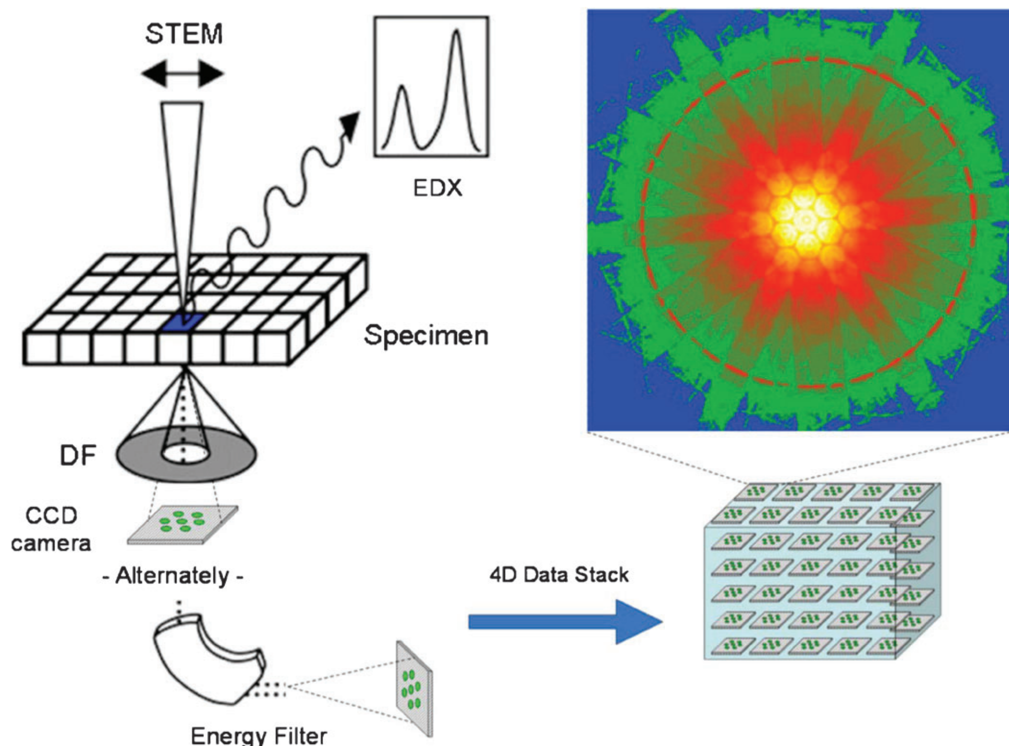

Fig. 4. Diffraction imaging concept. For each STEM probe position, a full diffraction pattern is recorded on a CCD camera or alternatively, through an energy filter. The resulting data form a 4D data set. Compatible signals such as EDS or HAADF data can be simultaneously acquired.

each containing 256 × 256 reciprocal space points would be around 8 Gb. To reduce the size of the file, it is possible to use a smaller camera length combined with a sub-area camera readout or to use line scan-based techniques.

Visualizing a 4D data stack on a 2D monitor is challenging. In addition to the acquisition techniques, tools have been developed to allow the visualization, manipulation and analysis of these 4D data sets.

STEM diffraction imaging combines the information-rich nature of electron diffraction with the spatially resolved power of spectrum imaging, enabling diffraction patterns to be acquired pixel by pixel as a 4D data set. In direct analogy with elemental mapping from spectrum images, any feature that can be measured from a diffraction pattern (e.g. lattice parameter, strain and composition) can, in principle, be mapped interactively from the acquired diffraction image data set. Further, acquisition can be performed simultaneously with other compatible signal streams (e.g. EDS). These and other possibilities make diffraction imaging a powerful technique for advanced sample characterization investigations.

Recent development in spectrum imaging data analysis

The density of states of a material is a complex function of local charges, atomic bonds and chemical constitution of the material; thus, measuring the density of state (DOS) provides a wealth of information beyond traditional microanalysis. Since the cross-section for inelastic scattering couples to the local density of states, the EELS signal will reflect these properties of the material (more precisely, the EELS cross-section couples to the symmetry projected, local density of empty states) [8]. Moreover, the anisotropy of the material and coupling to the momentum transfer of the scattered electron will make the cross-section depend on the local orientation of the sample with respect to the electron beam. Therefore, the EELS core-loss signal not only contains information about the chemical constitution of the material but also about the local environment of the atoms in the material. This feature allows the EEL spectrum to be used as a 'fingerprint' for the chemical phases in the material. The study of such kind of fine structure is called energy-loss near-edge structure or ELNES analysis [9]. From basic applications such as the distinction of Si and SiO_2 to the most advanced applications such as local charge determination or nanostructure analysis [10], ELNES is a very powerful and necessary tool for materials analysis. To analyze carefully the shape of the peaks, which can sometimes be overlapping, several computing tools have been developed as described below.

Multiple linear least-squares fitting

Multiple linear least-squares fitting (MLLS) has first been used by Leapman *et al*. [11] to separate overlapping core edges in EELS. MLLS can be used to fit a number of

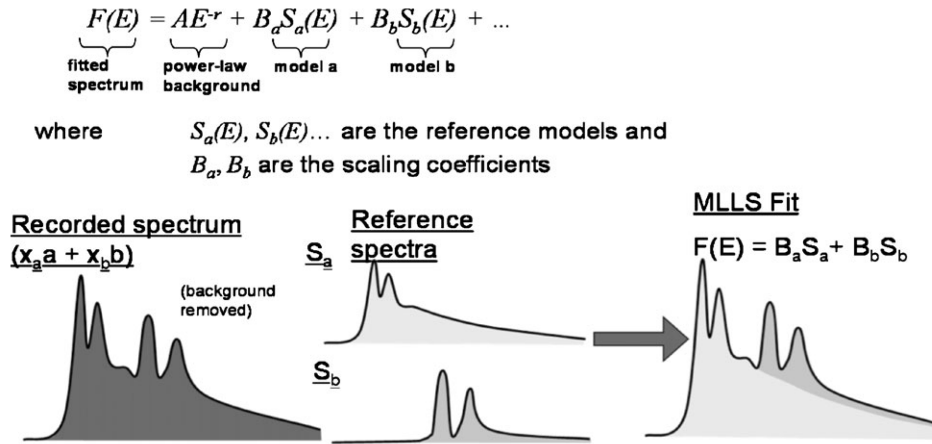

Fig. 5. MLLS fitting of a recorded spectrum containing components from two phases (A and B). With the background removed, the recorded spectrum can be decomposed in a sum of the two spectra $B_a.S_a(E)$ and $B_b.S_b(E)$. $S_a(E)$ and $S_b(E)$ are reference spectra corresponding to phases A and B. They can be either measured from a single phase area, taken from a database or even simulated. The MLLS fitting will evaluate the values of B_a and B_b corresponding to the amount of each phase (A and B) using a least-squares fitting and returning the value of χ^2 to evaluate the quality of the fitting. This MLLS fitting can be done on a spectrum-imaging file returning B_a and B_b for each scanned point resulting in mapping of chemical phases A and B.

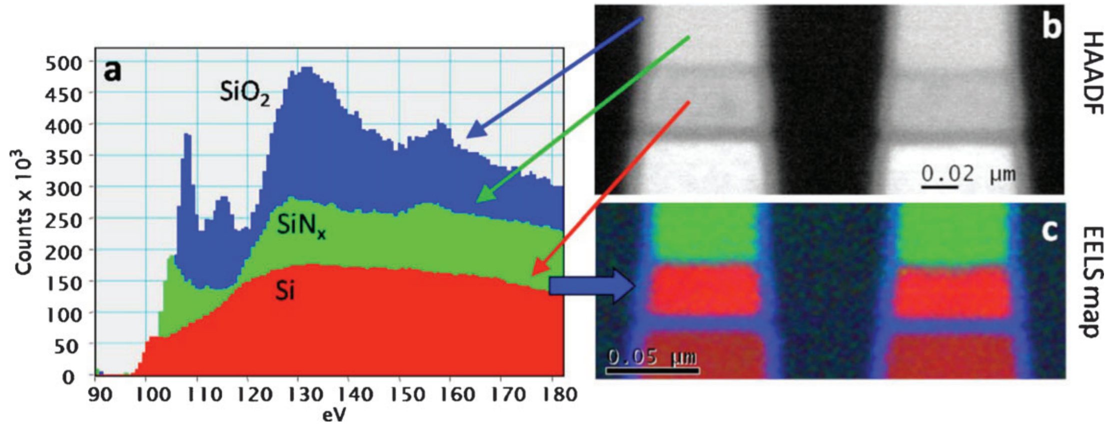

Fig. 6. Si $L_{2,3}$ effect of coordination. (a) shows the EELS spectra after background removal picked up from each of the three phases of this semiconductor sample: silicon, silicon nitride and silicon oxide. (b) shows the HAADF of the studied area of the sample. Si $L_{2,3}$ edge shape changes depending on the atom bonding and coordination of the Si atom. Thus, the edge shapes are different for SiO_2, SiN and Si making MLLS possible using the three reference spectra shown in (a). The result of the fitting is shown in (c) where points corresponding to SiO_2, SiN and Si are respectively shown in blue, green and red. We can see that each phase can be identified, even the nanometer thick layer of SiO_2 separating the SiN and Si. The experience has been done with an HD2300 with Enfina and STEM Pack.

reference spectra and/or models to an experimental spectrum as shown in Fig. 5. The reference spectra are used as fingerprints and should be preferably acquired on reference sample with the same equipment.

By combining MLLS and spectrum imaging, the ELNES analysis can be done not only on a singular spectrum but over a scanned area and results can be visualized as shown in Fig. 7, as color maps where phases correspond to each reference spectrum (or a reference chemical state). In order to focus on the fine structure itself, it is important to reduce as much as possible the unwanted part of the spectrum such as the background (easily removed by fitting it by a power law or a log-polynomial function) and the thickness effect (plural scattering). Thickness effects can be removed by techniques such as Fourier log, Fourier ratio deconvolution [12]. All those processes can be applied directly to the spectrum imaging data resulting in a newly treated spectrum imaging data set ready for MLLS analysis. Moreover, it can give us the reduced χ^2 corresponding to each pixel of the spectrum imaging showing us instantly if any chemical phase has been forgotten in the fitting and even where this phase can be found (by looking at the reduced χ^2 map).

As an example, we analyzed a semiconductor device containing silicon in three different forms of silicon: silicon dioxide, silicon nitride and crystalline silicon (Fig. 6). Since the density of states in each of those structures is very dissimilar, the silicon $L_{2,3}$ ELNES shape alone can be used to uniquely identify these phases. By picking reference spectra

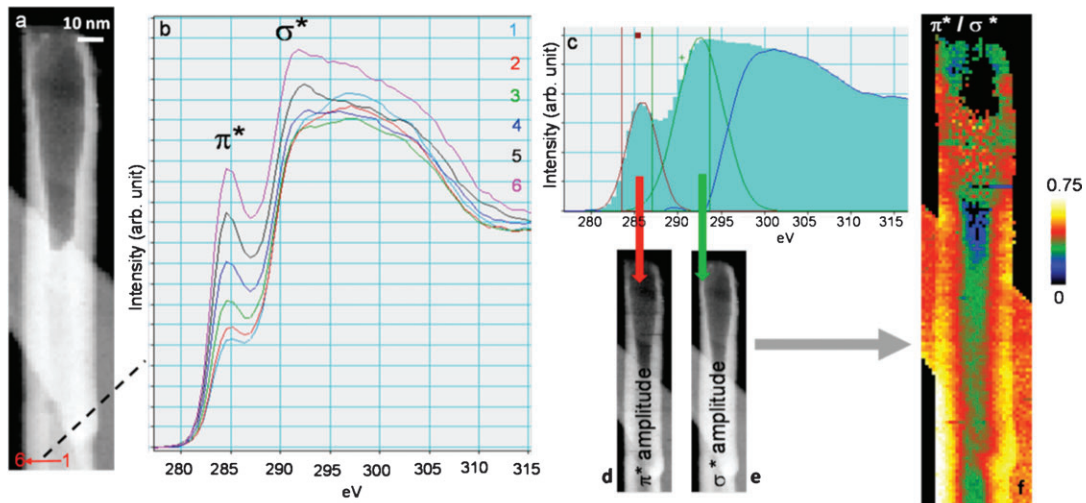

Fig. 7. Spectrum imaging analysis of the anisotropy effect in a 50-nm outer diameter MWCNT. (a) shows the HAADF of the MWCNT analyzed by SI. (b) shows the extracted spectrum, after the background has been removed, obtained from the center (1) to the side (6) of the tube. The anisotropy effect shows clearly a reduction of the π* peak at the center of the tube (1). (c) shows the NLLS fitting of the carbon K edge with Gaussian peaks in red and green to fit the π* peak and the σ* peak, respectively. The blue curve shows the residue of this fitting as discussed previously. The extracted amplitude for both π* and σ* is shown below in (d) and (e), respectively, and their ratio (f) exhibits the strong anisotropy effect expected. The intensity of the ratio is shown using the color scale shown next to (f) where the orange region represents the strong value of the π*/σ* ratio.

from each of those three phases, we can use MLLS fitting to obtain a very accurate phase map by looking at only the Si $L_{2,3}$ edge. This would have been impossible using traditional EELS analysis techniques [12].

Another advantage of the MLLS method is that it can easily separate overlapping peaks which are common in semiconductor devices (Si K edge starts at 1840 eV, while the broad, delayed M edges of Hf, Ta and W begin at 1660, 1735 and 1810 eV, respectively, making traditional signal extraction techniques problematic).

Non-linear least-squares fitting

The non-linear least-squares (NLLS) fitting tools allow one or more Gaussian peaks to be fitted to both a spectrum and every spectrum in an entire spectrum image. Once fitted, the fitting parameters can be output (amplitude, center, width) and displayed as 2D maps providing a powerful tool for mapping peak shifts in a spectrum image. This tool has been proved to be very useful to map the plasmon energy [13] by fitting the plasmon peak by a Gaussian function and identifying the plasmon energy as being the center of the Gaussian function. Other problems for which the NLLS fitting technique is well suited include mapping changed in the EELS white-line ratio for transition elements [14,15], for performing chemical shift measurements and for zero-loss alignment of low-loss EELS spectrum images.

NLLS fitting is not limited to white-line analysis; peaks such as O K and C K show a π^* (1 s→sp^2) peak very similar to a Gaussian function and even though their σ^* component does not show a Gaussian characteristic, it is possible to fit the beginning of the peak with a Gaussian curve and to use the intensity of the fitted function as a method to evaluate the σ^* component.

As an example, we measured a spectrum image from a multi-wall carbon nanotube (MWCNT). The ELNES of the carbon K edge in graphite shows a strong orientation dependence [16]. The amplitude of a π^* (1 s→sp^2) peak at 283 eV loss is modulated depending on whether sp^2 states are perpendicular or parallel to the e-beam. NLLS fitting to π^* and σ^* peaks allows a ratio map to be formed. As we can see in Fig. 7, we observe strong π^* on the side of the tube where the π^* states of the graphite are perpendicular to the incident electron beam. This method can be generalized to the study of any carbon-based material even for the amorphous carbon study [17]. Figure 7c shows a typical C K peak and how the NLLS fitting has been performed. We chose energy windows for both the π^* and the σ^* peaks so that the two Gaussian curves fit the experimental data within those windows. The σ^* component is not a sharp peak; therefore, the whole peak cannot be completely fitted, and the blue curve shows the residue of this fitting. However, we can clearly see that the blue curve is nearly null until an energy loss which is superior to 293 eV. In this particular example, this partial fitting actually increases the accuracy of our model since the shape of the C K peak of nanotubes for energies higher than 295 eV is strongly dependant on the tube's thickness.

As expected, we can see a high π^*/σ^* ratio where the beam is hitting the sample parallel to the graphite plane (the side of the tube). This enhanced ratio allows clear visualization of the wall thickness of the MWCNT. These measurements clearly show the anisotropy of the graphite bond and, in principle, can be directly used to measure the sp^2/sp^3 ratio; however, this is a much more challenging measurement as

demonstrated by Martin *et al.* [17]. Obtaining quantitative results required combining NLLS and MLLS techniques and a reference to a known sp^2/sp^3 ratio material. And as we saw previously, anisotropy effects can cause a very strong variation in the π^*/σ^* peak ratio for a constant sp^2/sp^3 material, making such measurements extremely challenging for anisotropic materials such as graphitic objects.

Multivariate analysis

Multivariate analysis is used to identify several base sources of information as contributing to the multivariate data set. A multivariate data set can be any data set described by a large number of variables such as an EELS spectrum image. This technique has first been used by Trebbia *et al.* [18] on an EELS line scan. In 2006, Bosman *et al.* [19] showed that multivariate analysis can be used on a spectrum image file. In our application, we use complementary chemical maps as a multivariate data set. Such an approach can offer the benefits of improved statistical relevance since the data set is treated as an ensemble, and unbiased (possibly automated) data analysis is achieved. Multivariate analysis facilitates a global view of the data set by projecting the data from a high-dimensionality space onto a space of reduced dimension. Besides aiding visualization, dimensionality reduction can also allow the rejection of noise and other redundant information.

Because spectrum images contain a large quantity of common information originating from specific physical sources, they are well suited to such analysis. The large data content in EELS–SI demands effective methods in data reduction and automated unbiased analysis tools. Moreover, EELS analysis searches for signals close to the detection limit, requiring tools for an optimal signal extraction.

To analyze multivariate data sets, it is useful to represent them as a multivariate histogram. It is a convenient way for revealing spatial correlations between multiple images, and allows mapping of phase relationships between complementary chemical distribution maps.

In the case of bivariate data sets, they would then be represented by a bivariate histogram where each axis corresponds to one data channel (i.e. one chemical element). For three variables, we should display the histogram as a 3D histogram cube, which is not convenient for manipulation. Therefore, we represent the trivariate histogram with a tertiary phase diagram as shown in Fig. 8a. Since the three constituent maps do not necessarily add to 100% per pixel, it is necessary to normalize them with respect to each other. This representation makes it difficult to quantify elements; however, it is informative qualitatively, and allows for an easy identification of different phases. To demonstrate the convenience and performance of a trivariate analysis, we analyze a semiconductor device using STEM–SI (Fig. 8).

We can clearly see different clusters in Fig. 8b. A technique called interactive correlation partitioning (ICP) can be used to trace back the identified phases to the original data, which retrieves the spatial distribution of contributing pixels [20–22]. The histogram regions (Fig. 8b) correspond to a well-defined phase. ICP trace-back yields a chemical-phase-specific map (Fig. 8c). Various selection tools can be used to define the region of interest in the histogram. Theoretical details about ICP can be found in Reference [21]. Basically, each point on the histogram corresponds to a real scanned pixel of the sample. Therefore, by selecting a cluster in the histogram, we are defining a spatial area on the sample which corresponds to a particular chemical phase. By visualizing the spectrum imaging data as a multivariate histogram, it is easy to identify noises or bad extraction points and therefore to obtain more accurate chemical maps.

Moreover, it is possible to automatically obtain phase-specific spectra (Fig. 8d) by averaging the spectra within the identified phases. For example, the sky blue area corresponds to a pure titanium area which is located between a layer of titanium oxide and one of titanium oxide mixed with aluminum. These results are corroborated by the extracted spectra where the sky blue spectrum shows only the Ti L_{23} edge. Without multivariate analysis, it would have been extremely difficult to exhibit all the seven phases in the sample. Moreover, it allows the saving of a considerable amount of time, usually used to probe the spectrum imaging looking for different phases. Being able to automatically sum all the spectra corresponding to a particular phase is a great tool to obtain a spectrum with a high signal-to-noise ratio that can further be used for ELNES analysis.

Mixing real and reciprocal space

As explained earlier, using diffraction imaging, it is possible to acquire diffraction pattern information at each pixel position and to analyze the obtained 4D data set in order to reconstruct an image in real space corresponding to a specific area in reciprocal space (diffraction pattern, CBED).

This technique is still new and only few results have already been obtained, but it opens up to new possibilities in materials analysis. Potential applications are ‘interactive’ bright-field and dark-field imaging done after acquisition or even element-selective imaging via selective *Z*-tuning done interactively post-acquisition. Other applications such as spatially resolved CBED studies, strain field or lattice parameter mapping or crystal orientation mapping are very promising.

The DI data are acquired with a CCD camera recording a micro-diffraction or CBED pattern while the sample is scanned. Once acquired, the DI can be viewed and manipulated within the digital micrograph environment. The information-rich content of a diffraction image requires a wide range of 4D visualization tools, which enable intuitive visualization and mapping of diffraction-pattern features in real time. Figure 9 shows a diffraction-image example taken from a semiconductor gate device. Using an ADF survey image (Fig. 9a), an energy-filtered diffraction image

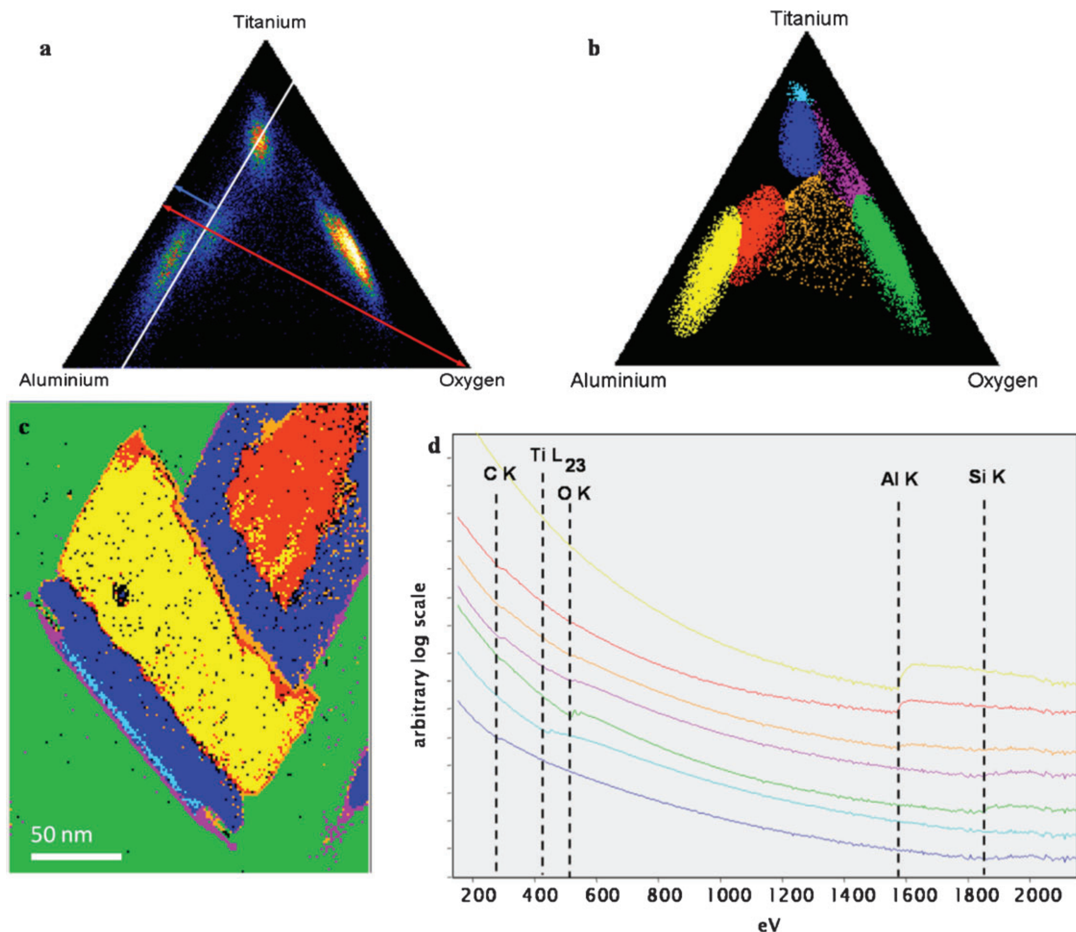

Fig. 8. Trivariate analysis of a semiconductor device. (a) The ratio of the length of the blue to that of the red line is indicative of the oxygen fractional contribution along the white line. We identify seven phases in the histogram (b) and select them using a hand-drawn selecting tool, appearing in different colors in the histogram after selection. We then trace back the corresponding pixels to construct a chemical-phase-specific map (c) using ICP. (d) shows phase-specific spectra obtained from each of the seven identified phases. The color of the spectrum lines corresponds to the color of the identified phases from (c).

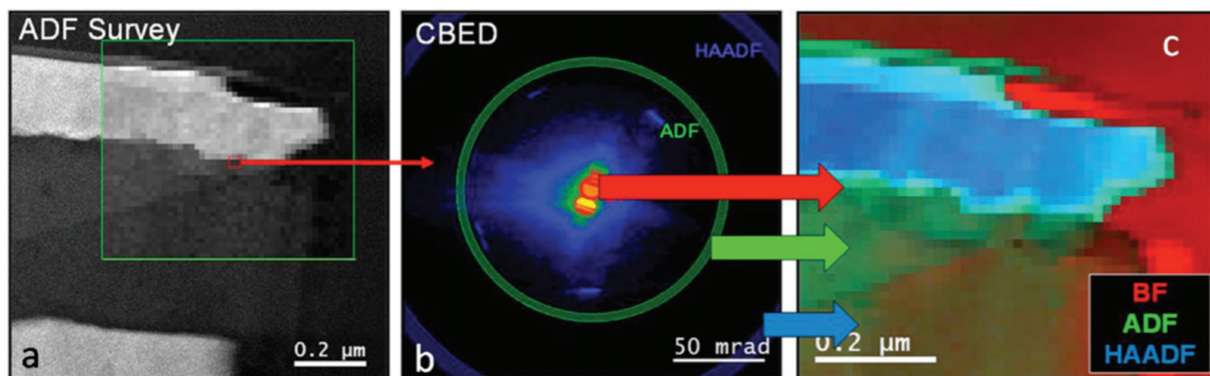

Fig. 9. Contrast tuning using diffraction imaging on a semi-conductor device. The DI scanning process has been done over the area delimited by a green square in the HAADF image (a). For each scanned point, the CBED pattern was measured with a 2048 × 2048 pixels camera used with an 8 times binning to increase the speed of the measurement and to reduce the size of the file, resulting in a 256 × 256 pixels CBED image for each of the 256 × 256 scanned pixels. (b) shows the extracted CBED pattern obtained from the area defined by the red square in (a). (c) shows an RGB composite image computed in this way composed of a bright-field (BF) image (red), the ADF image (green, 60–65 mrad) and the HAADF image (blue, 120–130 mrad) defined by the green and blue annuli in (b). These data were obtained using a JEOL 2010FasTEM with a Gatan GIF Tridiem detector.

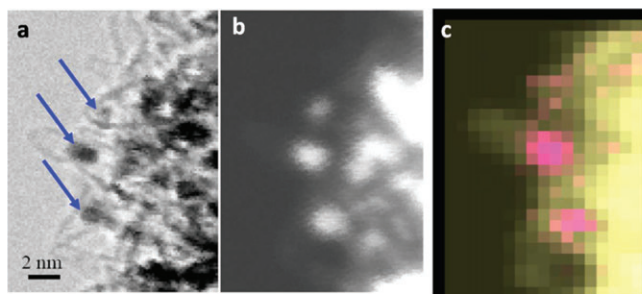

Fig. 10. EELS analysis of anticancer medicine (cisplatin) inserted inside a SWNH using fast scanning (10 s for a 30*20 map). (a) shows a bright-field image of some SWNHs containing CDDP nanoparticles inside (pointed out by the blue arrows). Those particles appear more clearly in the HAADF image (b) because the CDDP contains platinum which is very heavy compared to the surrounding carbon. The EELS map (c) acquired by the SI method shows clearly in pink the chloride from the CDDP surrounded by carbon from the nanohorns in yellow showing that the medicine has not been chemically altered by the beam during the measurement. Reprinted by permission of ACS, copyright 2008 [26].

was acquired from the region marked in green. A CBED pattern, extracted from the point marked in red, is shown in Fig. 9b. Using interactive 4D visualization tools, it is possible to generate an image from any feature or angular range in the diffraction space in real time. Figure 9c shows an RGB composite image computed in this way composed of a bright-field image (red), an annular dark-field (ADF) image (green, 60–65 mrad), and a high-angle annular dark field (HAADF) image (blue, 120–130 mrad). This colored image clearly shows the two structures contained in the gate appearing in green and blue. In the original ADF image, it was difficult to discern the difference between the two regions. By interactively tuning the angular range and observing the resulting image, it is possible to optimize the contrast between phases in the sample. This can be extended to as many regions as necessary in the data set. In the example given below, only three angular regions are needed to segment the five phases present in the sample.

The flexibility of the 4D visualization tools is very important for the experiment analysis. The selection can be done in either the real or reciprocal space using various kinds of selection tools, from a usual annular selection such as those shown in Fig. 9 to hand-drawn selection either in the reciprocal space to select a diffraction spot or in the real space to select a region of interest such as an interfacial region or a cluster.

DI is a very powerful tool but there are two limitations that require special care. First, the center of the diffraction pattern may shift during the acquisition, especially at low magnifications. The images should be realigned post-acquisition using the non-diffracted beam as a reference, and then the origin or diffraction pattern needs to be defined for the data set. Secondly, the optimization of the camera acquisition is made difficult by the large dynamic range of the diffraction pattern. Therefore, the acquisition time should be chosen carefully before acquisition to not saturate the camera. To increase the intensity of the measured signal without saturating the camera, it is possible to automatically rescan the studied area any number of times and sum the data at the end of the acquisition. This "multiple pass" scanning process can allow the detection of even a weak diffraction peak. This new process can also be used for EELS with spectrum imaging. This can help in the acquisition of the SI file of low-loss EELS spectra that can easily saturate the CCD detector if a short acquisition time is not used.

Discussion

Spectrum imaging shows an incredible versatility and accuracy. Atomic resolution EELS mapping can be obtained as shown in Fig. 1. Strong beam current, high-sensitivity detector, fast acquisition electronics and techniques such as sub-pixel scanning allow reduced the beam damage. This makes possible the study of beam-sensitive specimens such as medicines [23] or single-wall carbon nanotubes [24]. Figure 10 shows the EELS analysis of an anticancer medicine [cisplatin $PtCl_2(NH_3)_2$] inserted inside a single-wall carbon nanohorn (SWNH) [25], which is an aggregate of closed-end nanotubes (sample developed by K. Ajima and M. Yudaska from JST/SORST [26]). The black spots show the cisplatin molecules in the bright-field image. In the dark-field image, they are shown as bright regions because they contain platinum which is a heavy molecule (dark-field images are very sensitive to the local mass). The cisplatin medicine is very beam sensitive and without extra care the molecule changes into a non-effective molecule by losing its chloride atoms. The sample has been studied under an HD-2300 STEM from Hitachi equipped with a Gatan Enfina by scanning the area of interest for 10 s using sub-pixel scanning. For comparison, we tried to look at the same sample using EDX and an energy-filtered TEM, but in both cases, the time required to obtain an extractable chloride signal was too long and the cisplatin medicine was damaged resulting in the evaporation of the chloride atoms.

By acquiring EELS spectra with high-energy resolution over the studied area, spectrum imaging allows the application of EELS analysis tools such as MLLS and NLLS to obtain spatially resolved fine-structure results. Nelayah *et al*. showed in Reference [27] that optical properties can be analyzed by recording plasmon spectra in the near-infrared/visible/ultraviolet domain using electron beams instead of photons. Up to now, these measurements were generally limited to the ultraviolet spectral range (above 3 eV of energy loss) [28]. Without a monochromator, C. Colliex's team developed a method combining a Gatan spectrometer, Richardson–Lucy algorithm and customized acquisition process to be able to observe plasmon peaks below 2 eV extending the spectral range to the visible and the near-infrared domain. They applied this method to a equilateral Ag nanoprism with 78-nm-long sides and observed three

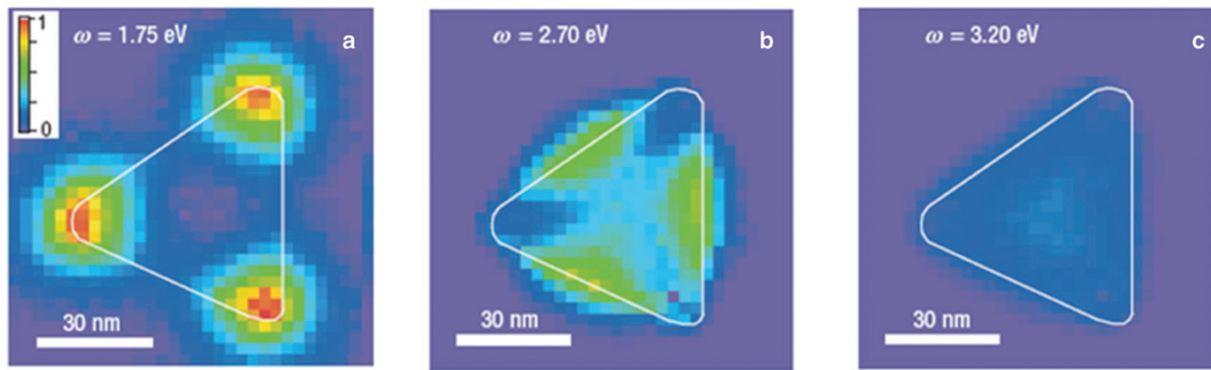

Fig. 11. Distribution of the modes centered at 1.75 (a), 2.70 (b) and 3.20 eV (c) respectively, in the spectra of an equilateral Ag nanoprism. For each spectrum, the amplitudes of the modes are measured at their corresponding maxima after subtraction of the zero-loss peak. The outer contour of the particle, deduced from its HAADF image, is shown as a white line. The color scale, common to the three maps, is linear and in arbitrary units. These results are consistent with the one obtained by EELS simulation of a similar nanotriangle [27]. Reprinted by permission from Macmillan Publishers Ltd: Nature Physics (http://www.nature.com/nphys/index.html), copyright 2007.

plasmon resonance modes centered at 1.75, 2.70 and 3.20 eV, corresponding respectively to wavelengths of 709, 459 and 3.87 nm [27].

Many applications in optoelectronics and nanophotonics, such as bio-sensing and cancer therapy, rely on optical excitations in metallic nanoparticles. Imaging the optical mode variation in those nanoparticles has been impossible for photonic spectroscopy which only provides averaged information over a whole population of nano-objects in a solution or on a substrate [29]. Recently, optical near-field microscopy showed that nano-objects can be analyzed but with a resolution limited to 50 nm [30]. Combining C. Colliex's method with spectrum imaging, his team showed that it is possible to map those plasmon resonance modes with a spatial resolution down to 10 nm allowing the mapping of the optical excitation mode within an equilateral Ag nanoprism with 78-nm-long sides as shown in Fig. 11.

The addition of diffraction imaging in the analytical electron microscopy world opens wide possibilities. During the electron scattering by the sample, two variables are affected, the energy of the incident electron and its scattered angle. EELS acquires the energy loss while DI explores the other axis, the angular distribution. For the first time, it is possible to obtain the complete information about the scattering process using an electron microscope. While the applications' possibilities still need to be explored, EELS/DI combinations are very promising. For example, DI analysis can be combined with chemical analysis provided by ELNES analysis, or change in a crystal structure, easily observed on a diffraction pattern, can be spatially correlated with the change in the ELNES.

Conclusion

Recent advances in SI allow the full advantage afforded by new-generation electron microscopes such as Cs-corrected STEM to be realized. The addition of new modalities such as sub-pixel scanning and multi-dimensional acquisition methods further enhances the power of these instruments. ELNES can easily be characterized using MLLS or NLLS data extraction techniques to reveal both the distribution of the atoms in the sample and the distribution of their chemical phase. Multivariate analysis is not only a very powerful method to perform state-of-the-art chemical characterization, but it is also a way toward automated and accurate material analysis. Diffraction imaging opens a new dimension to analytical electron microscopy and allows a more complete analysis of the scattering process (energy and scattering angle) to be obtained. While use of this method has just started, unprecedented experiments such as strain field or liquid crystal orientation mapping seems now possible.

Acknowledgements

The authors would like to thank M. Yudasaka (NEC/AIST Tsukuba), C. Colliex and M. Kociak (University Paris-Sud) as well as M. Pan, P. Thomas and M. Rabara from Gatan for their invaluable advices. They also thank Y. Zhu from Brookhaven National Laboratory. They would like to thank E. Okunishi from JEOL and H. Inada, S. Isakozawa, K. Nakamura from Hitachi High Tech for their support.

References

1 Colliex C (1996) New trends in STEM-based nano-EELS analysis. *J. Electron Microsc.* **45**: 44–50.

2 Batson P E (1995) Conduction band structure in strained silicon by spatially resolved electron energy loss spectroscopy. *Ultramicroscopy* **59**: 63–70.

3 Colliex C (2007) Microscopy: elementary resolution. *Nature* **450**: 622–623.

4 Muller D A, Fitting Kourkoutis L, Murfitt M, Song J H, Hwang H Y, Silcox J, Dellby N, and Krivanek O L (2008) Atomic scale chemical imaging of composition and bonding by aberration-corrected microscope. *Science* **319**: 1073–1076.

5 Williams D B, and Carter C B (1996) *Transmission Electron Microscopy. A Textbook for Materials Science*, pp 19–25 (Plenum, New York).

6 Colliex C, and Stephan O (2005). EELS: Methods, Theory and Applications. In: Wang Z L, and Yao N (eds), *Handbook of Microscopy for Nanotechnology*, pp 653–681 (Springer Verbg and Tsinghua Uni, New York).

7 Jonas L, Fulda G, Salameh T, Schmidt W, Kröning G, Hopt U T, and Nizze H (2001) Electron microscopic detection of copper in the liver of two patients with Morbus Wilson by EELS and EDX. *Ultrastruct. Pathol.* **25**(2): 111–118.

8 Egerton R F (1996) *Electron Energy-Loss Spectroscopy in the Electron Microscope*, 2nd edn, pp 227–243 (Plenum, New York).

9 Keast V J, Scott A J, Brydson R, Williams D B, and Brudley J (2001) Electron energy-loss near-edge structure: a tool for the investigation of electronic structure on the nanometre scale. *J. Microsc.* **203**: 135–175.

10 Yuge R, Yudasaka M, Maigné A, Tomonari M, Miyawaki J, Kubo Y, Imai H, Ichihashi T, and Iijima S (2008) Adsorption phenomena of tetracyano-p-quinodimethane on single wall carbon nanohorn. *J. Phys. Chem. C.* **112**: 5416–5422.

11 Leapman R D, and Swyt C R (1988) Separation of overlapping core edges in electron energy loss spectra by multiple-least squares fitting. *Ultramicroscopy* **26**: 393–404.

12 Johnson D W, and Spence J C H (1974) Determination of the single scattering probability distribution from plural-scattering data. *J. Phys. D* **7**: 771–780.

13 Porter A, Gass M, Muller K, Skepper N, Midgley P, and Welland M (2007) Direct imaging of single-walled carbon nanotubes in cells. *Nat. Nanotechnol.* **2**: 713–717.

14 Chen K-F, Lo S-C, Chang L, Egerton R, Kai J-J, Lin J-J, and Chen F-R (2007) Valence map of iron oxide thin film obtained from electron spectroscopy imaging series. *Micron* **38**(4): 354–361.

15 Riedl T, Gemming T, and Wetzig K (2006) Extraction of EELS white-line intensities of manganese compounds. Methods, accuracy, and valence sensitivity. *Ultramicroscopy* **106**: 284–291.

16 Stephan O, Kociak M, Henrard L, Suenaga K, Gloter A, Tence M, Sandre E, and Colliex C (2001) Electron energy-loss spectroscopy on individual nanotubes. *J. Electron Spectrosc. Relat. Phenomena* **114**: 209–217.

17 Martin P J, Filipczuk S W, Netterfield R P, Field J S, Whitnal D F, and Mckenzie D R (1988) EELS analysis of vacuum arc-deposited diamond-like films. *Philos. Mag. Lett.* **57**(6): 285–290.

18 Trebbia P, and Bonnet N (1990) EELS elemental mapping with unconventional methods I. Theoretical basis: Image analysis with multivariate statistics and entropy concepts. *Ultramicroscopy* **34**(3): 165–178.

19 Bosman M, Watanabe M, Alexander D T L, and Keast V J (2006) Mapping chemical and bonding information using multivariate analysis of electron energy-loss spectrum images. *Ultramicroscopy* **106**: 1024–1032.

20 Hofer F, Grogger W, Kothleitner G, and Warbichler P (1997) Quantitative analysis of EFTEM elemental distribution images. *Ultramicroscopy* **67**(1–4): 83–103.

21 Bonnet N, Herbin M, and Vautror P (1997) Multivariate image analysis and segmentation in microanalysis. *Scanning Microsc.* **11**: 1–21.

22 Kothleitner G, Rogers M, Berendes A, Bock W, and Kolbesen B O (2005) A combined SNMS and EFTEM/EELS study on focused ion beam prepared vanadium nitride thin films. *Appl. Surf. Sci.* **252**: 66–76.

23 Ajima K, Murakami T, Mizoguchi Y, Tsuchida K, Ichihashi T, Iijima S, and Yudasaka M (2008) Enhancement of in vivo anticancer effects of cisplatin by incorporation inside Single Wall Carbon Nanohorns. *ACSNano* **2**(10): 2057–2064.

24 Zobelli A, Gloter A, Ewels C P, Seiffert G, and Colliex C (2007) Electron knock-on cross-section of carbon and boron nitride nanotubes. *Phys. Rev. B* **75**: 245402.

25 Iijima S, Yudasaka M, Yamada R, Bandow S, Suenaga K, Kokai F, and Takahashi K (1999) Nano-aggregates of single-walled graphitic carbon nano-horns. *Chem. Phys. Lett.* **309**: 165–170.

26 Ajima K, Yudsaka M, Murakami T, Maigné A, Shiba K, and Iijima S (2005) Carbon nanohorns as anticancer drug carriers. *Mol. Pharm.* **2**: 475–480.

27 Nelayah N, Kociak M, Stephan O, Garcia de abajo O J, Tencé M, Henrard L, Taverna D, Pastoriza-Santos I, Liz-Marzan L M, and Colliex C (2007) Mapping surface plasmons on a single metallic nanoparticle. *Nat. Phys.* **3**: 348–353.

28 Arenal R, Stephan O, Kociak M, Taverna D, Loiseau A, and Colliex C (2007) Electron energy loss spectroscopy measurement of the optical gaps on individual boron nitride single-walled and multiwalled nanotubes. *Phys. Rev. Lett.* **95**: 127601.

29 Hao E, Schatz G C, and Hupp J T (2004) Synthesis and optical properties of anisotropic metal nanoparticles. *J. Fluoresc.* **14**: 331–341.

30 Sherry L, Mirkin C, Schatz G, and VanDuyne R (2006) Localized surface plasmon resonance spectroscopy of single silver triangular nanoprisms. *Nano Lett.* **6**: 2060–2065.